Swept source / Fourier domain polarization sensitive optical coherence tomography with a passive polarization delay unit

Article *in* Optics Express · April 2012

DOI: 10.1364/OE.20.010229 · Source: PubMed

6 authors, including:

Bernhard Baumann
Medical University of Vienna
110 PUBLICATIONS **1,679** CITATIONS
SEE PROFILE

Woojhon Choi
Massachusetts Institute of Technology
23 PUBLICATIONS **313** CITATIONS
SEE PROFILE

David Huang
Oregon Health and Science University
257 PUBLICATIONS **18,835** CITATIONS
SEE PROFILE

Jay Duker
Tufts Medical Center
389 PUBLICATIONS **13,686** CITATIONS
SEE PROFILE

Swept source / Fourier domain polarization sensitive optical coherence tomography with a passive polarization delay unit

Bernhard Baumann,[1,2] WooJhon Choi,[1] Benjamin Potsaid,[1,3] David Huang,[4] Jay S. Duker,[2] and James G. Fujimoto[1,*]

[1]*Department of Electrical Engineering and Computer Science, and Research Laboratory of Electronics, Massachusetts Institute of Technology, Cambridge, Massachusetts 02139, USA*
[2]*New England Eye Center and Tufts Medical Center, Tufts University, Boston, Massachusetts 02116, USA*
[3]*Advanced Imaging Group, Thorlabs, Inc., Newton, New Jersey 07860, USA*
[4]*Casey Eye Institute, Oregon Health & Science University, Portland, Oregon 97239, USA*
jgfuji@mit.edu

Abstract: Polarization sensitive optical coherence tomography (PS-OCT) is a functional imaging method that provides additional contrast using the light polarizing properties of a sample. This manuscript describes PS-OCT based on ultrahigh speed swept source / Fourier domain OCT operating at 1050nm at 100kHz axial scan rates using single mode fiber optics and a multiplexing approach. Unlike previously reported PS-OCT multiplexing schemes, the method uses a passive polarization delay unit and does not require active polarization modulating devices. This advance decreases system cost and avoids complex synchronization requirements. The polarization delay unit was implemented in the sample beam path in order to simultaneously illuminate the sample with two different polarization states. The orthogonal polarization components for the depth-multiplexed signals from the two input states were detected using dual balanced detection. PS-OCT images were computed using Jones calculus. 3D PS-OCT imaging was performed in the human and rat retina. In addition to standard OCT images, PS-OCT images were generated using contrast form birefringence and depolarization. Enhanced tissue discrimination as well as quantitative measurements of sample properties was demonstrated using the additional contrast and information contained in the PS-OCT images.

OCIS codes: (170.4500) Optical coherence tomography; (230.5440) Polarization-selective devices; (170.4580) Optical diagnostics for medicine; (170.4470) Ophthalmology.

References and links

1. M. R. Hee, D. Huang, E. A. Swanson, and J. G. Fujimoto, "Polarization-sensitive low-coherence reflectometer for birefringence characterization and ranging," J. Opt. Soc. Am. B **9**(6), 903–908 (1992).
2. J. F. de Boer, T. E. Milner, M. J. C. van Gemert, and J. S. Nelson, "Two-dimensional birefringence imaging in biological tissue by polarization-sensitive optical coherence tomography," Opt. Lett. **22**(12), 934–936 (1997).
3. S. M. Srinivas, J. F. de Boer, H. Park, K. Keikhanzadeh, H. E. L. Huang, J. Zhang, W. Q. Jung, Z. P. Chen, and J. S. Nelson, "Determination of burn depth by polarization-sensitive optical coherence tomography," J. Biomed. Opt. **9**(1), 207–212 (2004).
4. J. Strasswimmer, M. C. Pierce, B. H. Park, V. Neel, and J. F. de Boer, "Polarization-sensitive optical coherence tomography of invasive basal cell carcinoma," J. Biomed. Opt. **9**(2), 292–298 (2004).
5. P. O. Bagnaninchi, Y. Yang, M. Bonesi, G. Maffulli, C. Phelan, I. Meglinski, A. El Haj, and N. Maffulli, "In-depth imaging and quantification of degenerative changes associated with Achilles ruptured tendons by polarization-sensitive optical coherence tomography," Phys. Med. Biol. **55**(13), 3777–3787 (2010).
6. M. Pircher, C. K. Hitzenberger, and U. Schmidt-Erfurth, "Polarization sensitive optical coherence tomography in the human eye," Prog. Retin. Eye Res. **30**(6), 431–451 (2011).
7. M. Pircher, E. Götzinger, R. Leitgeb, H. Sattmann, O. Findl, and C. K. Hitzenberger, "Imaging of polarization properties of human retina in vivo with phase resolved transversal PS-OCT," Opt. Express **12**(24), 5940–5951 (2004).

#162775 - $15.00 USD Received 8 Feb 2012; revised 3 Apr 2012; accepted 14 Apr 2012; published 19 Apr 2012

8. E. Götzinger, M. Pircher, W. Geitzenauer, C. Ahlers, B. Baumann, S. Michels, U. Schmidt-Erfurth, and C. K. Hitzenberger, "Retinal pigment epithelium segmentation by polarization sensitive optical coherence tomography," Opt. Express **16**(21), 16410–16422 (2008).
9. C. Ahlers, E. Götzinger, M. Pircher, I. Golbaz, F. Prager, C. Schütze, B. Baumann, C. K. Hitzenberger, and U. Schmidt-Erfurth, "Imaging of the retinal pigment epithelium in age-related macular degeneration using polarization-sensitive optical coherence tomography," Invest. Ophthalmol. Vis. Sci. **51**(4), 2149–2157 (2010).
10. B. Baumann, E. Götzinger, M. Pircher, H. Sattmann, C. Schütze, F. Schlanitz, C. Ahlers, U. Schmidt-Erfurth, and C. K. Hitzenberger, "Segmentation and quantification of retinal lesions in age-related macular degeneration using polarization-sensitive optical coherence tomography," J. Biomed. Opt. **15**(6), 061704 (2010).
11. B. Cense, T. C. Chen, B. H. Park, M. C. Pierce, and J. F. de Boer, "Thickness and birefringence of healthy retinal nerve fiber layer tissue measured with polarization-sensitive optical coherence tomography," Invest. Ophthalmol. Vis. Sci. **45**(8), 2606–2612 (2004).
12. E. Götzinger, M. Pircher, B. Baumann, C. Hirn, C. Vass, and C. K. Hitzenberger, "Retinal nerve fiber layer birefringence evaluated with polarization sensitive spectral domain OCT and scanning laser polarimetry: a comparison," J Biophoton. **1**(2), 129–139 (2008).
13. M. Yamanari, M. Miura, S. Makita, T. Yatagai, and Y. Yasuno, "Phase retardation measurement of retinal nerve fiber layer by polarization-sensitive spectral-domain optical coherence tomography and scanning laser polarimetry," J. Biomed. Opt. **13**(1), 014013 (2008).
14. E. Götzinger, M. Pircher, M. Sticker, A. F. Fercher, and C. K. Hitzenberger, "Measurement and imaging of birefringent properties of the human cornea with phase-resolved, polarization-sensitive optical coherence tomography," J. Biomed. Opt. **9**(1), 94–102 (2004).
15. A. Miyazawa, M. Yamanari, S. Makita, M. Miura, K. Kawana, K. Iwaya, H. Goto, and Y. Yasuno, "Tissue discrimination in anterior eye using three optical parameters obtained by polarization sensitive optical coherence tomography," Opt. Express **17**(20), 17426–17440 (2009).
16. R. Leitgeb, C. K. Hitzenberger, and A. F. Fercher, "Performance of fourier domain vs. time domain optical coherence tomography," Opt. Express **11**(8), 889–894 (2003).
17. J. F. de Boer, B. Cense, B. H. Park, M. C. Pierce, G. J. Tearney, and B. E. Bouma, "Improved signal-to-noise ratio in spectral-domain compared with time-domain optical coherence tomography," Opt. Lett. **28**(21), 2067–2069 (2003).
18. M. A. Choma, M. V. Sarunic, C. H. Yang, and J. A. Izatt, "Sensitivity advantage of swept source and Fourier domain optical coherence tomography," Opt. Express **11**(18), 2183–2189 (2003).
19. B. Potsaid, I. Gorczynska, V. J. Srinivasan, Y. L. Chen, J. Jiang, A. Cable, and J. G. Fujimoto, "Ultrahigh speed spectral / Fourier domain OCT ophthalmic imaging at 70,000 to 312,500 axial scans per second," Opt. Express **16**(19), 15149–15169 (2008).
20. R. Huber, M. Wojtkowski, and J. G. Fujimoto, "Fourier Domain Mode Locking (FDML): A new laser operating regime and applications for optical coherence tomography," Opt. Express **14**(8), 3225–3237 (2006).
21. W. Y. Oh, B. J. Vakoc, M. Shishkov, G. J. Tearney, and B. E. Bouma, ">400 kHz repetition rate wavelength-swept laser and application to high-speed optical frequency domain imaging," Opt. Lett. **35**(17), 2919–2921 (2010).
22. B. Potsaid, B. Baumann, D. Huang, S. Barry, A. E. Cable, J. S. Schuman, J. S. Duker, and J. G. Fujimoto, "Ultrahigh speed 1050nm swept source/Fourier domain OCT retinal and anterior segment imaging at 100,000 to 400,000 axial scans per second," Opt. Express **18**(19), 20029–20048 (2010).
23. W. Wieser, B. R. Biedermann, T. Klein, C. M. Eigenwillig, and R. Huber, "Multi-megahertz OCT: High quality 3D imaging at 20 million A-scans and 4.5 GVoxels per second," Opt. Express **18**(14), 14685–14704 (2010).
24. V. Jayaraman, J. Jiang, H. Li, P. J. S. Heim, G. D. Cole, B. Potsaid, J. G. Fujimoto, and A. Cable, "OCT imaging up to 760 kHz axial scan rate using single-mode 1310nm MEMS-tunable VCSELs with >100nm tuning range," in *Lasers and Electro-Optics (CLEO), 2011 Conference on*, 2011), 1–2.
25. J. Zhang, W. Jung, J. S. Nelson, and Z. Chen, "Full range polarization-sensitive Fourier domain optical coherence tomography," Opt. Express **12**(24), 6033–6039 (2004).
26. M. K. Al-Qaisi and T. Akkin, "Swept-source polarization-sensitive optical coherence tomography based on polarization-maintaining fiber," Opt. Express **18**(4), 3392–3403 (2010).
27. M. Yamanari, S. Makita, and Y. Yasuno, "Polarization-sensitive swept-source optical coherence tomography with continuous source polarization modulation," Opt. Express **16**(8), 5892–5906 (2008).
28. W. Y. Oh, S. H. Yun, B. J. Vakoc, M. Shishkov, A. E. Desjardins, B. H. Park, J. F. de Boer, G. J. Tearney, and B. E. Bouma, "High-speed polarization sensitive optical frequency domain imaging with frequency multiplexing," Opt. Express **16**(2), 1096–1103 (2008).
29. P. Sharma, Y. Verma, K. D. Rao, and P. K. Gupta, "Single mode fiber based polarization sensitive optical coherence tomography using a swept laser source," J. Opt. **13**(11), 115301 (2011).
30. K. H. Kim, B. H. Park, Y. P. Tu, T. Hasan, B. Lee, J. A. Li, and J. F. de Boer, "Polarization-sensitive optical frequency domain imaging based on unpolarized light," Opt. Express **19**(2), 552–561 (2011).
31. C. K. Hitzenberger, E. Goetzinger, M. Sticker, M. Pircher, and A. F. Fercher, "Measurement and imaging of birefringence and optic axis orientation by phase resolved polarization sensitive optical coherence tomography," Opt. Express **9**(13), 780–790 (2001).
32. S. Jiao and L. V. Wang, "Jones-matrix imaging of biological tissues with quadruple-channel optical coherence tomography," J. Biomed. Opt. **7**(3), 350–358 (2002).
33. C. M. Fan, Y. Wang, and R. K. K. Wang, "Spectral domain polarization sensitive optical coherence tomography achieved by single camera detection," Opt. Express **15**(13), 7950–7961 (2007).

#162775 - $15.00 USD Received 8 Feb 2012; revised 3 Apr 2012; accepted 14 Apr 2012; published 19 Apr 2012

34. T. Schmoll, E. Götzinger, M. Pircher, C. K. Hitzenberger, and R. A. Leitgeb, "Single-camera polarization-sensitive spectral-domain OCT by spatial frequency encoding," Opt. Lett. **35**(2), 241–243 (2010).
35. S. G. Guo, J. Zhang, L. Wang, J. S. Nelson, and Z. P. Chen, "Depth-resolved birefringence and differential optical axis orientation measurements with fiber-based polarization-sensitive optical coherence tomography," Opt. Lett. **29**(17), 2025–2027 (2004).
36. B. Hyle Park, M. C. Pierce, B. Cense, and J. F. de Boer, "Jones matrix analysis for a polarization-sensitive optical coherence tomography system using fiber-optic components," Opt. Lett. **29**(21), 2512–2514 (2004).
37. S. Makita, M. Yamanari, and Y. Yasuno, "Generalized Jones matrix optical coherence tomography: performance and local birefringence imaging," Opt. Express **18**(2), 854–876 (2010).
38. M. Wojtkowski, V. J. Srinivasan, T. H. Ko, J. G. Fujimoto, A. Kowalczyk, and J. S. Duker, "Ultrahigh-resolution, high-speed, Fourier domain optical coherence tomography and methods for dispersion compensation," Opt. Express **12**(11), 2404–2422 (2004).
39. E. Götzinger, B. Baumann, M. Pircher, and C. K. Hitzenberger, "Polarization maintaining fiber based ultra-high resolution spectral domain polarization sensitive optical coherence tomography," Opt. Express **17**(25), 22704–22717 (2009).
40. B. Baumann, B. Potsaid, M. F. Kraus, J. J. Liu, D. Huang, J. Hornegger, A. E. Cable, J. S. Duker, and J. G. Fujimoto, "Total retinal blood flow measurement with ultrahigh speed swept source/Fourier domain OCT," Biomed. Opt. Express **2**(6), 1539–1552 (2011).
41. Z. H. Lu, D. K. Kasaragod, and S. J. Matcher, "Method to calibrate phase fluctuation in polarization-sensitive swept-source optical coherence tomography," J. Biomed. Opt. **16**(7), 070502 (2011).
42. G. J. Liu, J. Zhang, L. F. Yu, T. Q. Xie, and Z. P. Chen, "Real-time polarization-sensitive optical coherence tomography data processing with parallel computing," Appl. Opt. **48**(32), 6365–6370 (2009).
43. R. N. Weinreb, A. W. Dreher, A. Coleman, H. Quigley, B. Shaw, and K. Reiter, "Histopathologic validation of Fourier-ellipsometry measurements of retinal nerve fiber layer thickness," Arch. Ophthalmol. **108**(4), 557–560 (1990).
44. Q. Li, A. M. Timmers, K. Hunter, C. Gonzalez-Pola, A. S. Lewin, D. H. Reitze, and W. W. Hauswirth, "Noninvasive imaging by optical coherence tomography to monitor retinal degeneration in the mouse," Invest. Ophthalmol. Vis. Sci. **42**(12), 2981–2989 (2001).
45. N. Horio, S. Kachi, K. Hori, Y. Okamoto, E. Yamamoto, H. Terasaki, and Y. Miyake, "Progressive change of optical coherence tomography scans in retinal degeneration slow mice," Arch. Ophthalmol. **119**(9), 1329–1332 (2001).
46. T. Fukuchi, K. Takahashi, K. Shou, and M. Matsumura, "Optical coherence tomography (OCT) findings in normal retina and laser-induced choroidal neovascularization in rats," Graefes Arch. Clin. Exp. Ophthalmol. **239**(1), 41–46 (2001).
47. V. J. Srinivasan, T. H. Ko, M. Wojtkowski, M. Carvalho, A. Clermont, S. E. Bursell, Q. H. Song, J. Lem, J. S. Duker, J. S. Schuman, and J. G. Fujimoto, "Noninvasive volumetric imaging and morphometry of the rodent retina with high-speed, ultrahigh-resolution optical coherence tomography," Invest. Ophthalmol. Vis. Sci. **47**(12), 5522–5528 (2006).
48. M. Ruggeri, H. Wehbe, S. L. Jiao, G. Gregori, M. E. Jockovich, A. Hackam, Y. L. Duan, and C. A. Puliafito, "In vivo three-dimensional high-resolution imaging of rodent retina with spectral-domain optical coherence tomography," Invest. Ophthalmol. Vis. Sci. **48**(4), 1808–1814 (2007).
49. L. Duan, S. Makita, M. Yamanari, Y. Lim, and Y. Yasuno, "Monte-Carlo-based phase retardation estimator for polarization sensitive optical coherence tomography," Opt. Express **19**(17), 16330–16345 (2011).
50. M. Gora, K. Karnowski, M. Szkulmowski, B. J. Kaluzny, R. Huber, A. Kowalczyk, and M. Wojtkowski, "Ultra high-speed swept source OCT imaging of the anterior segment of human eye at 200 kHz with adjustable imaging range," Opt. Express **17**(17), 14880–14894 (2009).

1. Introduction

Polarization sensitive optical coherence tomography (PS-OCT) is one of the most promising functional extensions of OCT [1, 2]. By measuring the polarization properties of a sample in addition to reflectivity, PS-OCT provides additional contrast as well as quantitative measurements. In particular, PS-OCT has been demonstrated as a versatile tool for analyzing tissue integrity in vivo based on birefringence. While PS-OCT has been used in various biomedical applications ranging from burn depth estimation to cancer detection and collagen assessment [3–5], its most prominent use has been in ophthalmology [6].

In PS-OCT images of the eye, birefringent structures like the retinal nerve fiber layer (RNFL), depolarizing tissues like the retinal pigment epithelium (RPE) and polarization preserving structures like the photoreceptor layer, can be distinguished [7]. The depolarizing characteristic of the RPE can be used to segment this layer. The RPE is of specific interest in age-related macular degeneration (AMD) where this layer plays a key role in disease progression, but is often hard to identify solely based on its reflectivity in standard OCT images [8–10]. RNFL birefringence can be assessed using PS-OCT and might be an important marker for glaucoma diagnostics in addition to the nerve fiber layer thickness [11–13]. In the

#162775 - $15.00 USD Received 8 Feb 2012; revised 3 Apr 2012; accepted 14 Apr 2012; published 19 Apr 2012

anterior eye segment, structures such as sclera, conjunctive tissue and trabecular meshwork can be distinguished by their polarization properties [14, 15].

Recent technological advances have led to a significant increase in imaging speed and sensitivity using Fourier domain detection [16–18]. Using high speed line scan cameras in spectrometer based (spectral) Fourier domain OCT or frequency swept laser sources in swept source OCT, axial scan rates of several hundreds of kilohertz have been demonstrated [19, 20]. In clinical settings, rapid imaging speeds are important because they not only enable short imaging times, but also acquire more data in a shorter time. This facilitates volumetric imaging with reduced motion artifacts and the acquisition of densely sampled data sets. Speckle noise can be reduced and image contrast can be improved significantly by scanning the same cross-section repeatedly and averaging image frames.

The development of novel laser designs was a key technology for swept source / Fourier domain OCT. Polygon scanner based swept lasers, MEMS tuned laser sources, and Fourier domain mode locked lasers (FDML) with imaging speeds of several hundreds and even millions of wavelength sweeps per second have been reported [20–24]. Aside from high sweep repetition rates, many laser designs feature narrow instantaneous linewidths [22, 24]. In the Fourier domain, the narrow linewidths and corresponding long coherence lengths enable long imaging ranges with negligible sensitivity roll-off over several millimeters.

Several reports of swept laser based PS-OCT have been published, which cover a wide range of applications from ophthalmic to intravascular and endoscopic imaging [25–30]. In order to measure the polarizing properties of a sample with PS-OCT, the sample is usually illuminated with light of a known input polarization state using bulk optics or polarization-maintaining (PM) fiber implementations, and the OCT signal is measured with a polarization sensitive detection unit [1, 26, 31]. Bulk optics systems have the advantage that the input polarization state can be well defined and for this reason they have been used extensively in ophthalmic imaging. Fiber optic systems provide additional convenience and enable applications such as endoscopy or hand held probe based imaging, but have the disadvantage that the fiber causes a birefringent transformation of the polarization state, producing a variable input polarization state on the sample. For these reasons, in single mode fiber based systems, two different input polarization states with known relation are usually used in addition to polarization sensitive detection [2, 32]. This requires either sequential probing with two polarization states or multiplexing the two polarization states in one simultaneous axial scan acquisition. PS-OCT approaches using sequential illumination with two or more polarization states require oversampling, thus resulting in reduced acquisition rate and increased phase noise. Conversely, in multiplexing schemes, detection bandwidth and therefore image range is sacrificed in order to simultaneously detect the signals from the two incident polarization states. In bulk optics PS-OCT implementations with spectral/Fourier domain detection, PS detection used spatial frequency encoding and depth-multiplexing of the orthogonal detection channels [33, 34]. Impressive multiplexed approaches using swept source OCT have been demonstrated with polarization modulation and polarization state switching with electro-optic or acousto-optic devices [11, 27, 28, 35]. While proper encoding of the polarization states is crucial for these approaches, the addition of modulators adds to system cost and complexity by requiring sophisticated synchronization controls.

In this paper, we present an alternative approach to multiplexed PS-OCT at 100,000 axial scans per second based on swept source technology and single mode fiber optics. By employing a passive polarization delay unit, this scheme offers a simple, low cost and robust alternative to previously reported swept source PS-OCT methods including active electro-optic (EOM) and acousto-optic modulators (AOM). We demonstrate the system performance for retinal PS-OCT imaging in human subjects and exploit the high imaging speed to perform wide field imaging of the human retina. We also show PS-OCT images of the rat retina for the first time and investigate retinal polarization properties.

#162775 - $15.00 USD Received 8 Feb 2012; revised 3 Apr 2012; accepted 14 Apr 2012; published 19 Apr 2012

2. Methods

2.1 Experimental setup

A sketch of the experimental setup is shown in Fig. 1. The system was based on single mode fiber components (HI1060). A commercially available short cavity laser was used as a light source (Axsun Technologies, Inc.). The laser sweep range was 112.5nm and was centered at 1040nm. The sweep repetition rate of the laser was 100kHz. The laser emitted light during the forward sweep with a measured duty cycle of 58.2%. The average output power was 9.5mW. The laser output was split using a 90/10 coupler with 90% directed to the interferometer, while 10% was directed to a fiber Bragg grating (O/E Land, Inc.) centered at 989.976nm and used to generate a stable line trigger signal. The input to the interferometer was amplified using a semiconductor optical amplifier (SOA, Inphenix, Inc.) to provide a near-Gaussian spectrum centered at 1057nm with a FWHM bandwidth of 64nm with an average power of 23.5mW. An 80/20 coupler was used to separate sample and reference beams with 20% directed to a free-space reference delay, which included a retroreflector. The 80% arm was connected to a polarization controller and polarization delay unit (PDU), described in detail below (Fig. 1(B)).

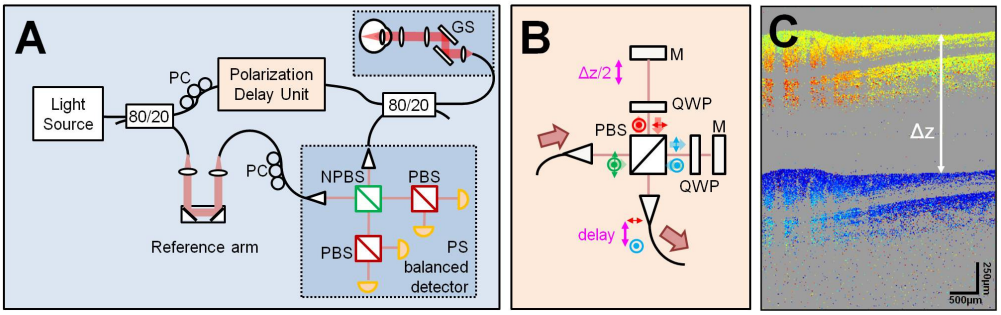

Fig. 1. Swept source / Fourier domain OCT with a passive polarization delay unit. (A) Scheme of the setup. In a single-mode fiber based Mach-Zehnder interferometer, a polarization delay unit is included in the sample illumination path. The sample and reference beam interfere at the non-polarizing beam splitter and are then split up into orthogonal polarization components by means of polarizing beam splitters. The two orthogonal polarization channels are detected by separate balanced receivers. (B) Scheme of the passive delay unit. (C) Exemplary image of the phase difference between the orthogonal detection channels. The OCT signals originating from the two incident states are separated by Δz = 1.8mm in depth. Acronyms: Polarization controller PC, galvanometer scanner GS, polarizing beam splitter PBS, non-polarizing beam splitter NPBS, quarter wave plate QWP, mirror M.

After the PDU, the sample arm light was split by a second 80/20 coupler, with 20% directed to the sample interface, including a pair of galvanometer scanners (Cambridge Technology 8315KM, mirror size: 5mm) and scanning optics (spot size at cornea: 1.8mm). For the human retinal imaging experiments, a slit lamp interface was used to aim the OCT beam into the eye. For PS-OCT imaging in rats, a different sample arm design (Cambridge Technology 6210H, mirror size: 3mm, spot size at cornea: 0.5mm) was used to accommodate the smaller geometry of the small animal eye. The power at the cornea was 1.3mW and 1.4mW for the human and rat interface, respectively. Light returning from the sample passed the 80/20 coupler and a collimator and interfered with the reference arm at a non-polarizing beam splitter. The spectral interference signal was then split into orthogonal polarization components using polarizing beam splitters at both outputs. The polarization of the reference arm was adjusted so that the two polarization channels had equal power. The signals for both channels were detected by two balanced detectors (Thorlabs, Inc.) and digitized with 12 bit resolution by a dual-channel digitizer (AlazarTech, Inc.) with a bandwidth of 500MHz. The acquisition was clocked by the k-clock generated by the laser source.

#162775 - $15.00 USD Received 8 Feb 2012; revised 3 Apr 2012; accepted 14 Apr 2012; published 19 Apr 2012

2.2 Polarization delay unit

The PDU enables simultaneous sample illumination with two orthogonal polarization states. In the PDU (Fig. 1(B)), light was collimated and split into orthogonal polarization components with a polarizing beam splitter (PBS). In either arm of the PDU, the polarization planes were rotated by 90° using an achromatic zero-order quarter wave plate (QWP) oriented at 45°, reflected by a mirror and reverse passed the QWP again. The two orthogonally polarized beams were recombined at the PBS and coupled into the output fiber leading to the sample interface. By adjusting the length difference between the two arms of the PDU to Δz/2, their overall sample arm lengths differed by Δz. Hence, OCT signals originating from each of the two orthogonal incident states appeared at depth positions separated by Δz in the OCT image (Fig. 1(C)). Using the delay unit, the two orthogonal channels were axially displaced by Δz = 1.8mm, such that each OCT signal covered approximately one half of the total image range of 3.8mm (in air). A sensitivity of ~94dB was measured using a neutral density filter (OD 2.5) and a mirror.

2.3 Data processing

Jones analysis was used to compute the PS-OCT images [36, 37]. For each detection channel, the acquired spectral signals were processed using standard Fourier domain OCT routines including background subtraction, numerical dispersion compensation, zero padding and Fourier transforming to compute the complex-valued OCT signals [38].

In order to de-multiplex the OCT signals separated by Δz, a mirror was used as a calibration target to match the path lengths between the depth-multiplexed channels. Depth-matching can be performed in the Fourier domain by adding first-order dispersion to one of the channels [27]. Similarly, path-matching can be performed directly in the spatial domain by shifting one channel along the z-axis [39]. We chose the latter approach for matching the path length between the multiplexed channels. Proper shifting was controlled by computing the phase difference between the signals originating from different depth positions. The path match accuracy by shifting by integer pixels is ~3.9μm after direct Fourier transform of the spectrum, and ~2.7μm and ~1.3μm after zero-padding once and twice, respectively (assuming a refractive index of n = 1.38 in tissue). In general, depending on the PDU design, the optical path of the two depth-multiplexed signals may have different higher order dispersion as well as path length and dispersion can be compensated numerically for each of the channels.

Assuming equal reference arm power in both channels, the four complex signals from the horizontal (H) and vertical (V) detection channel can be written as two complex field vectors,

$$E^1_{meas} = \begin{pmatrix} H_1 \\ V_1 \end{pmatrix}, E^2_{meas} = \begin{pmatrix} H_2 \\ V_2 \end{pmatrix} \tag{1}$$

where 1 and 2 denote the signals originating from the two orthogonal incident states multiplexed in depth (omitting a multiplicative constant)

$$E^1_{in} = \begin{pmatrix} 1 \\ 0 \end{pmatrix}, E^2_{in} = \begin{pmatrix} 0 \\ 1 \end{pmatrix}. \tag{2}$$

The field vectors at the surface of the sample were found using a segmentation algorithm described earlier [40]. Analogous to Eq. (2), the surface vectors are related to the input field vectors via the Jones matrices of the input path J_{in} and the output path J_{out}:

$$E^{1,2}_{surf} = J_{out} J_{in} E^{1,2}_{in}. \tag{3}$$

Signals from inside the sample are also subject to the roundtrip Jones matrix of the sample, J_{sample}:

$$E^{1,2}_{meas} = J_{out} J_{sample} J_{in} E^{1,2}_{in}. \tag{4}$$

#162775 - $15.00 USD Received 8 Feb 2012; revised 3 Apr 2012; accepted 14 Apr 2012; published 19 Apr 2012

Now, since $\left[E_{in}^{1}\ E_{in}^{2}\right]=\begin{bmatrix}1 & 0\\ 0 & 1\end{bmatrix}$, the measured Jones matrix in each image pixel can simply be reconstructed from the two measured field vectors:

$$J_{meas}=\left[E_{meas}^{1}\ E_{meas}^{2}\right]=J_{out}J_{sample}J_{in}. \tag{5}$$

By referencing the Jones matrix J_{meas} of an image pixel inside the tissue to the Jones matrix $J_{surf} = J_{out}J_{in}$ measured at the surface, the birefringence of the fiber components and anterior sample polarization can be compensated. For every image pixel, the unitary transform of the Jones matrix of the sample J_{sample} can be computed as [36, 37, 41]:

$$J_{sample}^{U}=J_{out}J_{sample}J_{out}^{-1}=J_{meas}J_{surf}^{-1}. \tag{6}$$

From this Jones matrix, the polarization properties of the sample can be computed. In order to analyze depolarizing tissue properties, we employed the Stokes vector based analysis described in ref [8]. In brief, the Stokes vector elements were calculated from the amplitudes and the phase difference of the measured field vectors. The uniformity of Stokes vector elements was then evaluated by computing the degree of polarization uniformity (*DOPU*) for every image pixel [8]

$$DOPU=\sqrt{Q_{mean}^{2}+U_{mean}^{2}+V_{mean}^{2}} \tag{7}$$

where Q_{mean}, U_{mean}, and V_{mean} denote the average of the respective normalized Stokes vector elements for small kernels. It should be noted that the spatial image resolution is somewhat reduced by averaging dependent on the kernel size. The choice of the kernel size is a trade-off between covering a large enough number of speckles for DOPU calculation and sufficient DOPU image resolution. For these studies, dimensions of 22.5(X) × 27.0(Y) μm^2 were used for averaging. DOPU values close to 1 indicate tissue with uniform polarization states such as polarization-preserving (e.g., photo receptor layer) and birefringent tissues (e.g., RNFL), whereas lower DOPU values are associated with depolarizing tissues. The lower DOPU values due to polarization scrambling in pigmented structures like the RPE can be used as a tissue-inherent contrast for segmentation of this layer [8].

Data processing was performed using single-threaded MATLAB code and took 2-5 minutes from raw data to stacks of PS-OCT B-scan images and en-face maps. Processing could be sped up by parallel computing as well as GPU implementations [42]. This could enable real-time PS-OCT imaging for clinical applications.

3. Results

3.1 High speed volumetric imaging

Retinal PS-OCT imaging was performed in the eyes of healthy human volunteers. The study protocol adhered to the tenets of the Declaration of Helsinki and was approved by the Committee on Use of Humans as Experimental Subjects (COUHES) at MIT. Written informed consent was obtained prior to the study. The study protocol for small animal imaging (section 3.3) was reviewed and approved by the Committee on Animal Care (CAC) at MIT.

For imaging the human retina, scan acquisition times are usually limited by eye motion and eye blinking. In clinical OCT systems, typical acquisition times for a volumetric data set are in the range of 2-3 seconds. Imaging with ultrahigh speed OCT enables the acquisition of similarly sampled data sets in much shorter time, allowing the acquisition of virtually motion-free OCT volumes. Alternatively, three-dimensional imaging with dense, isotropic sampling is possible within standard scan acquisition times.

#162775 - $15.00 USD Received 8 Feb 2012; revised 3 Apr 2012; accepted 14 Apr 2012; published 19 Apr 2012

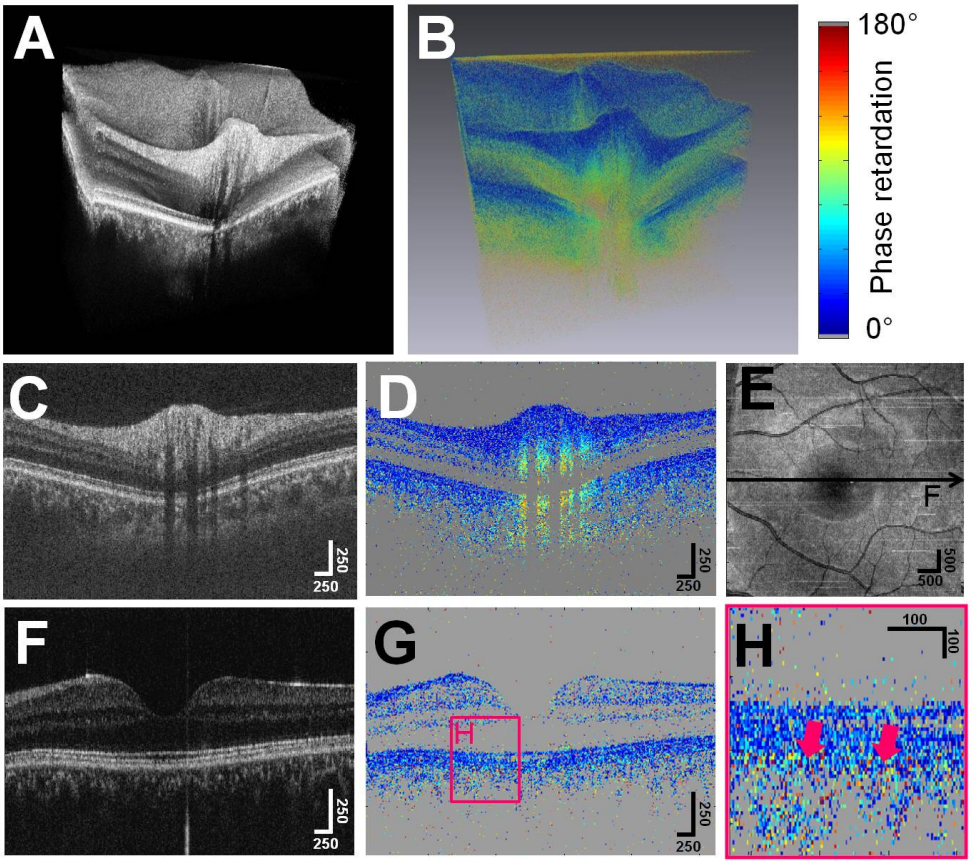

Fig. 2. High speed volumetric PS-OCT imaging in the human retina. (A-D) Snapshot PS-OCT imaging of the optic disk region. (A) Volumetric rendering of a 3D reflectivity data set. (B) Rendering of the corresponding phase retardation data. Increasing phase retardation can be observed in the birefringent RNFL. (C) Reflectivity B-scan image. (D) Corresponding phase retardation image. Phase retardation values between 0° and 180° are encoded in a color map ranging from blue to red. Image pixels below a reflectivity threshold are displayed in grey. (E-H) PS-OCT imaging of the macula with dense sampling. (E) OCT fundus projection image. (F) Reflectivity B-scan image. (G) Phase retardation image. (H) Detail of (G) showing the polarization preserving photoreceptor layer and polarization scrambling in the RPE (purple arrows). All scale bars in microns.

High speed volumetric imaging was performed by recording data sets of 500 × 100 axial scans. Retinal imaging was performed with an incident average power of 1.3mW, consistent with American National Standards Institute (ANSI) standards safe exposure limits. With the swept source / Fourier domain OCT system, the acquisition time for such a data set is only ~0.55 seconds, accounting for the galvonometer fly-back time. Snapshot PS-OCT imaging results of the optic disk region are shown in Fig. 2. Figures 2(A) and 2(B) show volume renderings of the reflectivity and phase retardation data, respectively. Corresponding B-scan images are shown in Figs. 2(C) and 2(D), respectively. Increasing phase retardation from the RNFL birefringence can be observed in the phase retardation B-scan image.

PS-OCT imaging with isotropic sampling (500 × 500 axial scans over 5 × 5mm^2) is demonstrated in the fovea region (Fig. 2). All retinal layers visualized in high resolution OCT can be distinguished in the reflectivity image (Fig. 2(F)). The retardation images of the fovea provide additional contrast (Figs. 2(G) and 2(H)). Figure 2(G) exhibits rather uniform phase retardation in most retinal layers (Fig. 2(G)). A zoom-in of the phase retardation image reveals the polarization preserving photoreceptor layer and the depolarizing pigment epithelium (Fig. 2(H)) [7]. Polarization scrambling in the RPE can be observed as varying

#162775 - $15.00 USD Received 8 Feb 2012; revised 3 Apr 2012; accepted 14 Apr 2012; published 19 Apr 2012

phase retardation values manifesting in a spotted appearance of this layer with varying colors (indicated by purple arrows in Fig. 2(H)).

3.2 Wide field PS-OCT imaging of the human retina

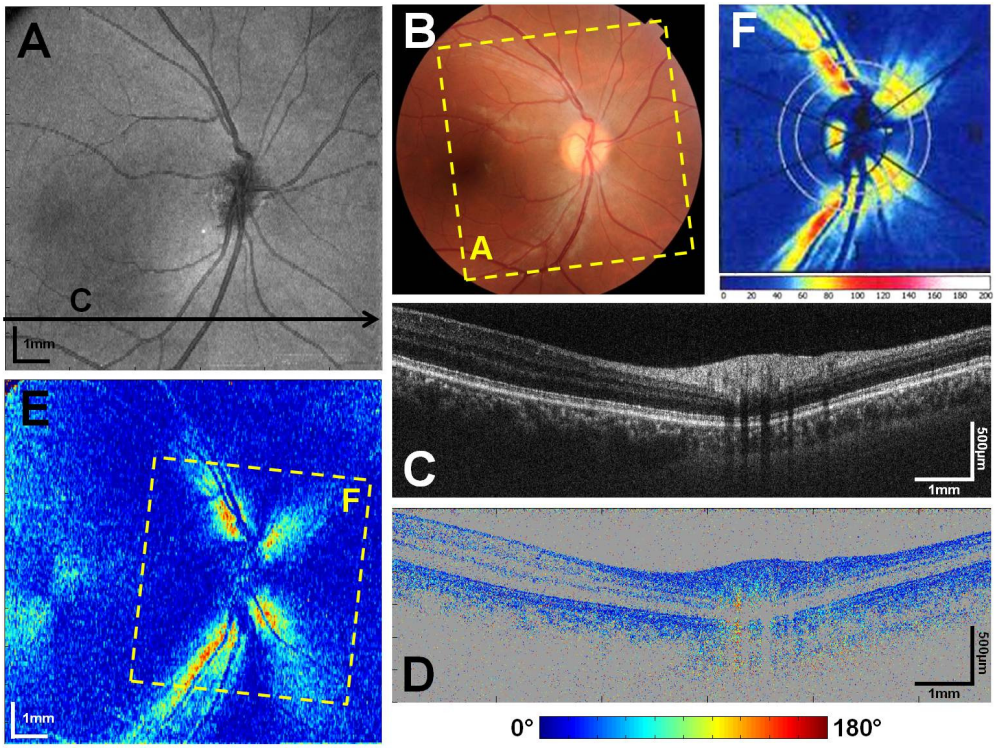

Fig. 3. Wide field PS-OCT imaging of the human retina. (A) Fundus projection image. As indicated in the color fundus photo (B), the scanned area covers a range of 26° × 26° on the retina. (C) Reflectivity B-scan image on the location indicated by the arrow in (A). (D) Corresponding phase retardation image (color scale: 0°– 180°). Increasing phase retardation due to RNFL birefringence can be observed by a color change from blue to yellow. (E) Wide field fundus image of phase retardation (color scale: 0° – 27°). Strong birefringence can be observed around the optic disk along the nerve fiber bundles. (F) Scanning laser polarimetry image of the same eye taken with the Zeiss GDx. Color map below. The scanned area of 15° × 15° is indicated by the dashed rectangle in (E).

The high imaging speeds of the swept source PS-OCT system enable the acquisition of retinal data sets covering a wide field of view. An OCT fundus projection image generated from a 3D volume of 1000 × 250 axial scans acquired in 2.78 seconds covering 26° × 26° is shown in Fig. 3(A). The scanned area is indicated on the color fundus photo (Fig. 3(B)). A reflectivity B-scan image extracted from the same data volume is shown in Fig. 3(C). RNFL birefringence can be observed as a color change from blue to yellow in the corresponding phase retardation image (Fig. 3(D)).

A fundus phase retardation map is shown in Fig. 3(E). In this map, the birefringent RNFL is clearly visible around the optic disk. Some interaction between the birefringent Henle's fiber layer and uncompensated birefringence of the cornea can be observed in the fovea region. A similar retardation pattern around the optic disk can be observed in the RNFL map generated with a commercial scanning laser polarimeter, the Zeiss GDx (Fig. 3(F)). The GDx raster-scans a laser beam over the retina and converts phase retardation value measured for each lateral position into a RNFL thickness value by assuming a fixed conversion factor, i.e. assuming constant birefringence in the RNFL [43]. For example, the GDx image of the healthy retina in Fig. 3(F) indicates RNFL thickness values between 0µm (blue) and ~110µm

#162775 - $15.00 USD Received 8 Feb 2012; revised 3 Apr 2012; accepted 14 Apr 2012; published 19 Apr 2012

(red). Using the same conversion, the wide field retardation image computed from the PS-OCT data set can be interpreted as RNFL thickness map (blue: 0µm; red: 117µm). However, when comparing the two images, it must be noted that the GDx and the PS-OCT system operate at different wavelengths so that different phase retardances can be expected, and that the respective color maps are also different.

3.3 PS-OCT imaging in the rat retina

Animal models are an important for research in disease pathogenesis and the development of new therapeutics for retinal diseases such as AMD, glaucoma or diabetic retinopathy. While histology is the gold standard for these types of studies, OCT has been applied in small animal studies and pathologic changes in the retina can be visualized in rodents in vivo, allowing longitudinal as well as cross-sectional studies [44–48]. Here, we investigate PS-OCT for imaging the rat retina.

Retinal imaging was performed in male Sprague Dawley rats and Long Evans rats (weight: 250–300g) with the swept source PS-OCT system. The rats were anesthetized with isoflurane (2%) and xylazine (8mg/kg). Pupil dilation was achieved by topical application of tropicamide (1%) on the eye. PS-OCT data sets with 1000 × 250 and 500 × 500 axial scans covering areas of 1.0 × 1.0mm^2 and 1.5 × 1.5mm^2 were recorded. The acquisition time for these data sets is only 2.78 seconds.

Results of imaging in a Sprague Dawley rat and in a Long Evans rat are shown in Fig. 4. The OCT fundus projection images show the vessel pattern around the optic disk (Figs. 4(A) and 4(F)). Cross-sectional reflectivity images reveal the structural differences between the retinal anatomy of the albino rat (Sprague Dawley, Fig. 4(B)) and the pigmented rat (Long Evans, Fig. 4(G)). Figure 4(C) and 4(H) show details of these B-scans.

In the Sprague Dawley rat, the RPE appears as a thin hyperreflective line, while the choroidal vessels appear as dark pattern (Fig. 4(C)). Deep light penetration into the sclera is evident. In contrast, the RPE and choroid of the pigmented Long Evans rat appear as a highly scattering complex (Fig. 4(H)). Due to the strong attenuation in these layers, less light penetrates into the sclera. Imaging with PS-OCT shows that while the retinal and choroidal structures appear polarization preserving in the Sprague Dawley rat, the collagen-containing sclera exhibits high birefringence manifesting in an increase of phase retardation with depth (Fig. 4(D)). In contrast, the pigmentation of the RPE/choroid complex in the Long-Evans rat causes polarization scrambling (Fig. 4(J)). This polarization scrambling effect can also be observed in the DOPU images (Figs. 4(E) and 4(K)). In the albino Sprague Dawley rat retina, high DOPU values close to 1 indicate rather uniform polarization states in all layers, which manifests in reddish color (Fig. 4(E)). While the retinal layers show a similar characteristic in the DOPU image of the pigmented Long Evans rat, color changes from red to yellow and green can be observed in the pigmented structures of the RPE/choroid complex (Fig. 4(K)).

3.4 Fiber based polarization delay unit

The PDU described in section 2.2 is used to generate different delays for orthogonally polarized light. However, since the PDU design is based on bulk optics, it suffers from losses when coupling back into the fiber. In order to reduce this loss, we developed a PDU based on polarization maintaining (PM) fibers (Fig. 5), which is described in this section.

#162775 - $15.00 USD Received 8 Feb 2012; revised 3 Apr 2012; accepted 14 Apr 2012; published 19 Apr 2012

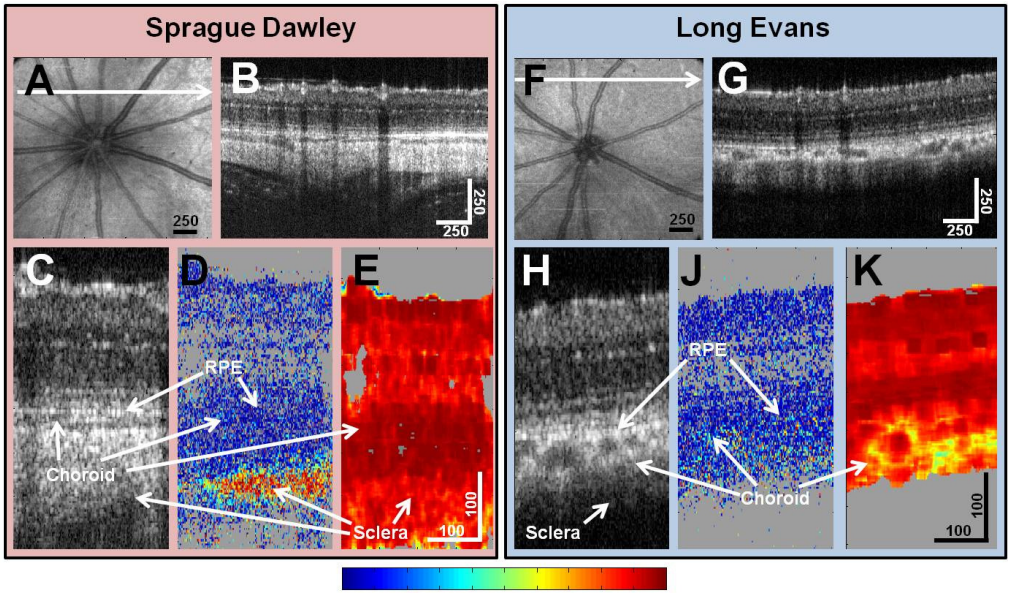

Fig. 4. Retinal PS-OCT imaging in rats. (A-E) Sprague Dawley rat. (F-K) Long Evans rat. (A, G) Fundus projection images showing the retinal vasculature around the optic disk. (B, C) Reflectivity B-scan images. (C, H) Retinal cross-section details. (D, J) Phase retardation images (color scale: 0° – 180°). PS-OCT reveals polarization properties distinguishing the birefringent sclera and polarization scrambling only in the pigmented RPE and choroid of the Long Evans rat. (E, K) DOPU images (color scale: 0 – 1). Polarization scrambling in the RPE/choroid complex of the pigmented rat manifests in lower DOPU values (yellow, green). All scale bars in microns.

PM fibers have different refractive indices along their two orthogonal axes (Fig. 5(B)). The phase delay between the two polarization states is proportional to the beat length of the PM fiber (i.e., to the difference between the refractive indices, Δn), and the fiber length. Assuming a PM fiber with length L and beat length L_B, a polarization dependent delay $\Delta z = \lambda \cdot L/2L_B$ is induced between the orthogonal channels (Fig. 5(C)). The factor ½ accounts for single pass of the fiber in the sample arm.

As a proof of principle, a 5m patch cord of PM fiber (PM980-XP, Nufern Inc., beat length: 2.7mm) was used in the sample arm of the PS-OCT system. For λ = 1050nm, the displacement in the image can be calculated as $\Delta z = \lambda \cdot L/2L_B$ = 1050nm·5m/(2·2.7mm). The measured insertion loss was only ~1dB, compared with ~3dB in the bulk PDU. The increased efficiency of the fiber based PDU enables using different coupler ratios and/or light sources with lower power. Example images from the PM fiber based delay unit are shown in Fig. 5. The signals from one detection channel (log amplitude) are shown in Fig. 5(D). The signals originating from the orthogonally polarized incident states, i.e., from the two channels of the PM fiber, appear at different depths separated by Δz = 0.97mm in the raw image, which is sufficient for retinal imaging. By splicing specific lengths of PM fibers into the system, the polarization offset Δz can be tailored for the respective system and application. PS-OCT images of reflectivity and phase retardation are shown in Figs. 5(E) and 5(F). These images demonstrate an imaging performance of the PM fiber based system similar to the retinal images acquired using the bulk PDU (Fig. 2).

4. Discussion and conclusion

A new, simplified scheme for swept-source PS-OCT based on single-mode fiber optics was presented. Single mode fiber based PS-OCT approaches generally require at least two different incident polarization states in order to retrieve the polarization information for PS-

#162775 - $15.00 USD Received 8 Feb 2012; revised 3 Apr 2012; accepted 14 Apr 2012; published 19 Apr 2012

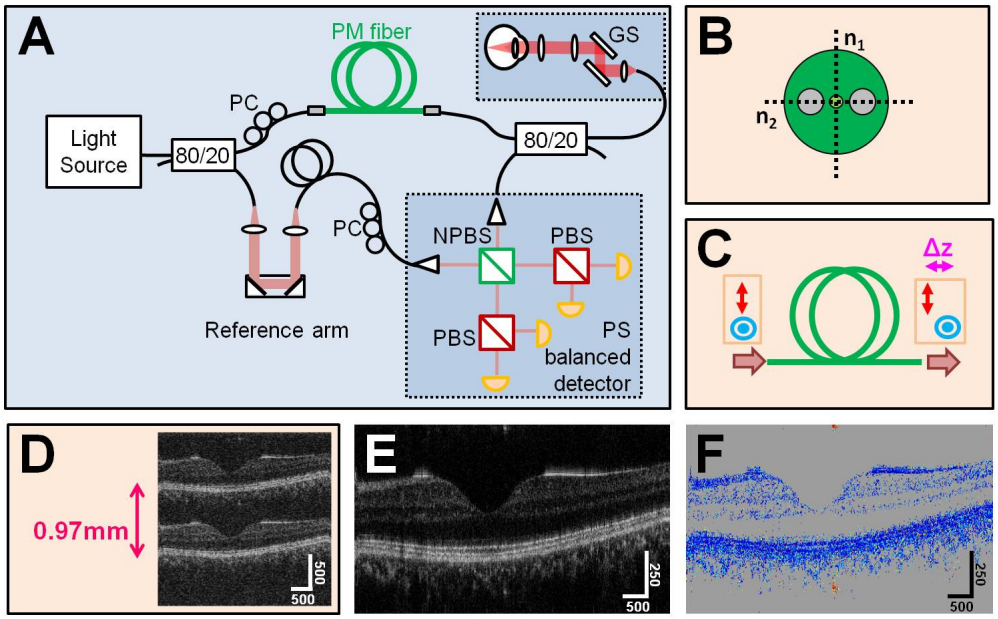

Fig. 5. PM fiber based delay for polarization multiplexing. (A) A PM fiber patch cable was inserted in the sample illumination arm of the interferometer. (B) PM fibers have different refractive indices, n_1 and n_2, along their two polarization channels. (C) The refractive index difference causes a delay Δz between its orthogonal polarization channels. (D) The OCT signals originating from these two orthogonal incident states appear displaced by $\Delta z = 0.97$mm for a 5m long PM fiber in the sample arm. (E) Reflectivity B-scan image. (E) Phase retardation image.

OCT images. In our approach, a passive polarization dependent delay unit was added in the sample arm. The PDU induces different sample arm path lengths for orthogonally polarized light, thus enabling to detect the polarization sensitive information for two incident states simultaneously. Previous approaches based on swept source / Fourier domain OCT and single mode fiber optics required active modulators such as EOMs and AOMs in either the sample or reference arm to encode two (or more) incident polarization states. These devices not only add to system cost, but also significantly increase system complexity since they require dedicated high speed control and exact triggering.

Compared to the passive multiplexing method presented here, swept-source PS-OCT approaches using active modulators may also have the inherent drawbacks due to their design: Acousto-optic modulators and frequency shifters often have low diffraction efficiencies, thus requiring higher light source power. The modulation efficiency of EOMs can be polarization dependent. For example, in a swept-source PS-OCT system using an EOM for polarization multiplexing, the SNRs of the modulated channels were reported to be 8-10dB lower than the SNRs of their non-modulated counterparts [49]. Furthermore, many active modulators are operated in a resonant mode in order to achieve modulation frequencies on the order of several tens or hundreds of MHz. Resonant devices as well as devices that operate at a single frequency have limited flexibility and may be a bottleneck for multimodal OCT systems with adjustable imaging range [50]. In contrast, in the PDU design described in section 2.2, the depth range may be adjusted by simply shifting one of the mirrors,

Different parameters may impact the efficiency of the PDU. Both the bulk PDU and the PM fiber based PDU may differ in efficiency between the two polarization channels due to polarization mode dependent coupling, polarization dependent attenuation, or residual attenuation of one channel caused by sensitivity roll-off with depth. In order to avoid any impact of the signal level difference between the two polarization channels on PS-OCT image

#162775 - $15.00 USD Received 8 Feb 2012; revised 3 Apr 2012; accepted 14 Apr 2012; published 19 Apr 2012

quality, equal signal levels were assured by careful polarization adjustment of the light input into the PDU.

Our approach overcomes most of the limitations of previously reported PS-OCT techniques with two incident states. However, compared to PS-OCT approaches using only a single input state, methods with two incident states have an inherent sensitivity loss of 3dB per state, since laser safety standards allow only half the probing power for each of the two states. Therefore, high system efficiency is required. However, after the first 80/20 splitter (1dB), the PDU (3dB), the second 80/20 splitter (6.9dB), and the sample interface optics (1dB), only ~5.5% of the input light arrive at the sample. The use of the 80/20 coupler in the sample arm of the system poses a problem when light source power is limited. This shortcoming could be overcome by using a circulator in the sample arm to enable more efficient use of the light source power. Moreover, the PDU described in section 2.2 was based on bulk optics and there was a measured insertion loss of ~3dB due to coupling out and back into single mode fibers.

In order to enhance the performance of the bulk optics PDU, we implemented a fiber based PDU, which reduced insertion loss from ~3dB to ~1dB. The images shown in Fig. 5 demonstrate that the PM fiber based approach could further simplify multiplexed PS-OCT and increase efficiency. While the system cost and complexity for the bulk PDU described in section 2.2 is already only a fraction of that in EOM or AOM based schemes, a PM fiber delay can further reduce cost and complexity.

In this article, we demonstrated a new swept-source PS-OCT system and demonstrate its application to retinal imaging. PS-OCT is a promising tool for assessing RNFL birefringence and polarization scrambling in the RPE. To our knowledge, PS-OCT was demonstrated the first time in the rat retina. We showed that the additional contrast provided by PS-OCT allows distinguishing highly birefringent structures like the sclera from polarization preserving tissue or depolarizing tissues like the RPE and choroid. Depolarization caused by pigments can be used as a tissue intrinsic contrast, and was not observed in albino rats, which lack pigment. Hence, PS-OCT may be useful for future studies of small animal models of retinal degeneration and other diseases.

Depth multiplexed PS-OCT takes advantage of the long coherence length of state-of-the-art swept lasers and has the potential to become the method of choice for future PS-OCT systems based on inexpensive single mode fibers. PS-OCT has been demonstrated for many applications in ophthalmology and its additional contrast and ability to quantitatively assess tissue properties may make it a promising tool for imaging applications in other fields. In particular, PS-OCT may be useful for fiber based applications such as endoscopic or intravascular imaging. Since the scheme presented in this article is based on single mode fibers, it could easily be implemented using existing catheters and endoscopic probes.

Acknowledgments

The authors thank Dr. Ireneusz Grulkowski, Jonathan J. Liu, Chen Lu, and Martin Kraus at MIT, as well as Dr. Allen C. Clermont, and Dr. Edward P. Feener at Joslin Diabetes Center for discussions and technical assistance. We gratefully acknowledge Lauren Branchini and Dr. Caio Regatieri at Tufts Medical Center for assistance with fundus imaging, as well as Drs. Andrea Cruzat and Rony Sayegh at Mass Eye and Ear for help with GDx imaging. We thank Dr. Alison Hayward and Wayne Au for helpful advice for animal handling. We also acknowledge support from the National Institutes of Health (NIH R01-EY011289-25, R01-EY013178-12, R01-EY013516-09, R01-EY019029-04, R01-EY018184-05, R01-CA075289-14, R01-HL095717-03, R01-NS057476-05), Air Force Office of Scientific Research (AFOSR FA9550-10-1-0063), Medical Free Electron Laser Program (FA9550-07-1-0101), and materials support by Thorlabs, Inc. Dr. Bernhard Baumann was visiting from the Center for Medical Physics and Biomedical Engineering, Medical University of Vienna, Austria.

#162775 - $15.00 USD Received 8 Feb 2012; revised 3 Apr 2012; accepted 14 Apr 2012; published 19 Apr 2012